Oxidative reactivity of alkali-like superatoms of group 5 metal-encapsulating Si_{16} cage nanoclusters

Masahiro Shibuta [1], Toshiaki Kamoshida[2], Tsutomu Ohta[2], Hironori Tsunoyama [2] & Atsushi Nakajima [1,2]

It is crucial to control the reactivity of surface silicon atoms for applications in miniaturized silicon-based nanodevices. Here we demonstrate that reactive silicon atoms are made unreactive by forming a Si_{16} cage that encapsulates a metal atom. Specifically, group 5 metal-encapsulating Si_{16} nanoclusters (M@Si_{16}: M = V, Nb, and Ta) exhibit alkali-like superatomic behavior on n-type C_{60} substrates, where charge transfer between M@Si_{16} and C_{60} satisfies the 68-electron shell closure as M@Si_{16}^+. The oxidation properties of M@Si_{16}^+ are investigated by X-ray photoelectron spectroscopy, revealing that the chemical stability of the caged silicon surface towards oxygen is enhanced by a factor of 10^4 compared to a crystalline silicon surface, and that M@Si_{16} are oxidized stepwise from the outer Si_{16} cage to the central metal atom. While the nanoclusters share a common Si_{16} cage, their chemical robustness depends on a superatomic "periodicity" (Ta@Si_{16} > V@Si_{16} > Nb@Si_{16}) which is explained by the electron density distributions of M@Si_{16} investigated by DFT calculations.

[1] Keio Institute of Pure and Applied Sciences (KiPAS), Keio University, 3-14-1 Hiyoshi, Kohoku-ku, Yokohama 223-8522, Japan. [2] Department of Chemistry, Faculty of Science and Technology, Keio University, 3-14-1 Hiyoshi, Kohoku-ku, Yokohama 223-8522, Japan. Correspondence and requests for materials should be addressed to A.N. (email: nakajima@chem.keio.ac.jp)

Silicon is the most important element in the development of modern technology. The demands of the latest functional devices (e.g. to be lightweight, flexible, energy saving, etc.) make it especially important that the functional units are constructed to be as small as possible, on the nanometer scale[1,2]. Since miniaturization of functional units with conventional patterning methods like photolithography has almost reached its limit[3], it is urgent that we discover methods to construct Si-based low-dimensional functional nanomaterials (e.g. silicon nanodots, nanowires, nanosheets) that are fabricated with bottom-up technologies utilizing fine synthesis methods in the gas and liquid phases[4–9], where each silicon nanomaterial is regarded as a building block of functionality. Furthermore, from a material science perspective, the chemical stability of the fabricated silicon nanomaterials is also very important because the surface oxidation reaction in the nanomaterials often changes their original functions. Therefore, strategies to make Si-based nanomaterials chemically robust are indispensable. In particular, chemical reactivity towards reactive oxygen gas is a common issue in the development of practical nanodevices and is also worth comparing to that of naked Si crystalline surfaces that exhibit an extremely reactive dangling-bond of Si atoms.

Silicene, a counter part of graphene, is a two-dimensional (2D) functional nanomaterial with Si atoms, achieving high in-plane conductivity combined with flexibility[9–13]. Although the Si atom, unlike the C atom, preferably forms sp^3 hybridized chemical bonds, the 2D conformation of silicene forces it to make sp^2-like Si−Si bonds, resulting in a nonflat 2D network (buckling structure)[9–12]. In spite of the structural deviation from the ideally flat sp^2 conformation (cf. graphene), an enhancement of chemical robustness towards oxygen has been reported for silicene, which reaches a factor of 10^3 as compared to that of sp^3 bonded crystalline Si[11,12]. To make a stable Si compound with "zero dimensional" nanostructure, by analogy with C_{60} fullerene, one can assume that a rounded silicene will have stable caged surface. From this viewpoint, much experimental and theoretical research on the simplest Si caged materials have been conducted, including Si_{60}[14–17]. However, such a stable caged Si compound has not so far been clearly identified, although the Si compound is highly expected to work in harmony with well-established Si nanotechnology.

Making a nanoscale rounded Si surface, i.e. caged Si, with metal encapsulation is one promising approach to realize chemically stabilized Si-based functional compounds[18–36]. Here the central metal atom enhances the electronic stability of the Si cage by sharing their valence electrons to form a superatom[30,33–36]. In fact, transition metal-encapsulating Si_{16} nanocluster superatoms ($M@Si_{16}$) can be synthesized in the gas phase, exhibiting a magic number behavior like a C_{60} fullerene[23,27]. Since their chemical properties can be tuned by choosing a different metal atom in the center of the geometrically close-packed $M@Si_{16}$, the assembly of a series of $M@Si_{16}$ could be a pathway to building Si-based nanomaterials.

In the literature, there are two electron counting rules for "superatoms"[26,28,29,34,36] and "18-electrons"[19,21,25,30] to explain the electronic properties of $M@Si_n$. Including a charge state, the electronic stabilities of $M@Si_{16}$ (M = Sc, Ti, and V) are governed by their superatomic nature and exhibit a shell-closure of 68 electron $(16 \times 4 \ e^- \ (Si) + 4 \ e^- \ (M) = 68 \ e^-)$[26,28,29,34,36]. In addition, the extended 18-electron rule can contribute to form $M@Si_n$ (n = 12, 14, and 16)[19,21,25,30]. In the DFT calculations for $Ti@Si_{16}$[34], its Kohn−Sham orbitals demonstrate that the $3s$ and $3p$ orbitals of the Si atoms are delocalized into superatomic orbitals, where the 68-electron shell closure, $(1S)^2(1P)^6(1D)^{10}(1F)^{14}(2S)^2(1G)^{18}(2P)^6(2D)^{10}$, governs their enhanced stability as found experimentally in gas phase[27,28]. In addition, a part of

electronic states in the calculated Kohn−Sham orbitals can also be described by 18-electron filling to the $4s$, $4p$, and $3d$ orbitals of the central Ti atom. Since the two electron counting rules of "superatoms" of 68 electrons and "18-electrons" for a transition metal atom are not exclusive to each other, both may contribute to stabilizing the $M@Si_{16}$ superatoms.

Since the group-5 transition metals V, Nb, and Ta possess five valence electrons, the $M@Si_{16}$ superatom (M = V, Nb, and Ta) is stabilized as cationic species as $M@Si_{16}^+$ to satisfy the 68-electron shell[23,27,34,36–41], and therefore the $M@Si_{16}$ neutrals are classified as alkali-like superatoms. In addition, the Si cages that include a group-3 atom (M = Sc, Y, and Lu) or a group-4 atom (M = Ti, Zr, and Hf) exhibit halogen-like and rare gas-like behaviors in a superatom periodic table[23,27,34,36].

We previously reported the chemical characterization of $Ta@Si_{16}$ deposited on a graphite substrate as a demonstration of the use of X-ray photoelectron spectroscopy (XPS) to element-specifically clarify the local electronic structure of the caged Si atoms[39], although the analysis of the chemical reactivity was qualitative and the species were limited to $Ta@Si_{16}$ in an alkali-like superatomic family.

Here we provide chemical characterization of alkali-like superatoms, including group 5 central atoms, to demonstrate periodicity in a superatom periodic table together with quantitative kinetic analyses for oxidation reactions which suggest metal-dependent superatom chemistry. The degree of chemical robustness of these $M@Si_{16}$ superatoms, which is about 10^4 higher than a naked crystalline Si surface, depends on the central metal atom: $Nb@Si_{16}$ is the most reactive owing to the electron density spreading outside the Si_{16} cage, as suggested by DFT calculations.

Results

Generation and deposition of $M@Si_{16}^+$. Figure 1 shows the mass spectra of cationic M−Si binary nanoclusters (Fig. 1a, M = V, Fig. 1b, Nb, and Fig. 1c, Ta) generated with a magnetron sputtering (MSP) method[34,36,42]. In the mass region of 400−700 m/z, a series of $M_1Si_n^+$ ions are predominantly observed. Although the series of Si_n^+ and $M_2Si_n^+$ are observed as minor products especially for M = Nb (as marked in the figure) those species are almost negligible around the $M@Si_{16}^+$ region. Optimizing the production conditions of Ar and He flows and sputtering power, the $M@Si_{16}^+$ signals prominently appear as magic numbers; $V@Si_{16}^+ = 500 \ m/z$, $Nb@Si_{16}^+ = 542 \ m/z$, and $Ta@Si_{16}^+ = 630 \ m/z$. Although the MSP method usually generates cold nanoclusters with less magic number behavior compared to those made with a laser vaporization method[23,27,34,36,42], the typical ion currents of generated $M@Si_{16}^+$ were larger than 500 pA with enhanced ion currents compared to their neighbors, as shown in Fig. 1. The flux of 3×10^9 clusters/s (at 500 pA) can deposit an amount of 1 monolayer (ML) on a substrate within 4 h, where the coverage is defined by the total ion current, and the amounts in the deposition area are consistent with those evaluated with step-by-step XPS measurements for C $1s$ and ultraviolet photoelectron spectroscopy (UPS) for C_{60}-derived signals (Supplementary Figures 1 and 2). For XPS measurements, the peak profiles derived from the core levels of Si and M elements remain the same for coverages in the range of 0.3−1.4 ML, while the increase in their intensities show saturation behavior at >1 ML (Supplementary Figure 3), and $M@Si_{16}^+$ is typically deposited to 0.6 ML in all XPS analyses.

Chemical environment of $M@Si_{16}$ on C_{60}. Figure 2 shows the XPS spectra for $V@Si_{16}$, $Nb@Si_{16}$, and $Ta@Si_{16}$ deposited on the C_{60} substrate (photon energy ($h\nu$) = 1253.6 eV), where the
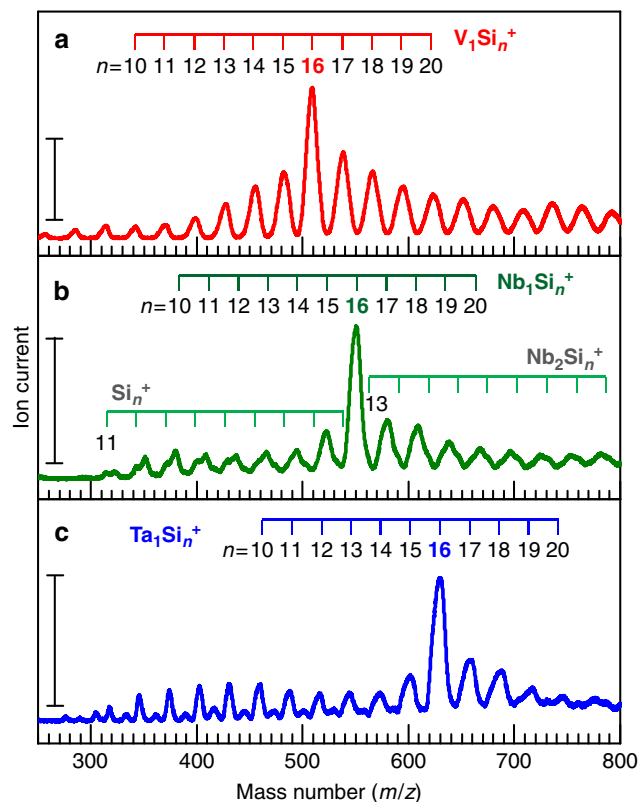
Fig. 1 Mass spectra of M_mSi_n binary nanocluster cations. The mass spectra for **a** V_mSi_n, **b** Nb_mSi_n, and **c** Ta_mSi_n cations show that the series of $M_1Si_n^+$ ions (marked in the figures for $n = 10-20$) are mainly generated with a magic number behaviors of $M@Si_{16}^+$. The vertical scale bars represent ion currents of 500 pA, and all $M@Si_{16}^+$ are larger than 500 pA. While Si_n^+ and $M_2Si_n^+$ are also resolved for M = Nb and Ta with minor products, those are negligible around the $M@Si_{16}^+$ region

Fig. 2 XPS spectra for $M@Si_{16}$ superatom deposited on a C_{60} substrate. The binding energies are around core levels of Si 2p for **a** $V@Si_{16}$, **b** $Nb@Si_{16}$, and **c** $Ta@Si_{16}$, and metal core levels of **d** V 2p for $V@Si_{16}$, **e** Nb 3d for $Nb@Si_{16}$, and **f** Ta 4f for $Ta@Si_{16}$. Reference binding energies of Si $2p_{3/2}$ for bulk Si (Si^0), and M (V $2p_{2/3}$, Nb $3d_{5/2}$, and Ta $4f_{7/2}$) for M^0 and M^{2+} are marked by vertical bars. Their binding energies show zerovalent Si and monovalent M^+

binding energy regions encompass the core levels of Si 2p (Fig. 2a −c) and central metal atoms (Fig. 2d; V 2p, 2e; Nb 3d, and 2f; Ta 4f). Since all XPS signals derived from Si and M increase linearly with the deposition up to 1 ML (Supplementary Figure 3), all $M@Si_{16}$ are nondestructively immobilized on the C_{60} substrate without forming three-dimensional aggregates, consistent with scanning tunneling microscopy (STM) observations[37,38]. Using an instrumental broadening (Voigt peak function; full width at half maximum (FWHM) = 1.09 eV with Lorentzian and Gaussian widths of 0.56 eV and 0.75 eV, respectively), the peaks of Si 2p core level are deconvoluted into two components which are due to spin-orbit splitting ($2p_{2/1,3/2}$) with a known peak separation (0.608 eV) and branching ratio of 2J+1 (1:2)[43]. As seen in Fig. 2, the peak reproductions of Si 2p for all $M@Si_{16}$ indicate that the chemical environment of Si atoms composing $M@Si_{16}$ is uniform within the energy resolution of the XPS measurements; this implies that the surrounding Si atoms are almost equally distributed around the central metal atoms. Compared to the binding energy of Si $2p_{3/2}$ for bulk Si (99.5 eV)[44], the Si $2p_{3/2}$ peaks for all $M@Si_{16}$ at 99.6−99.7 eV indicates that the charge states of the surrounding Si atoms are close to that of bulk Si (Si^0). Note that a small extra-component at a higher binding energy is seen for the Si 2p peak for $Nb@Si_{16}$, which is presumably caused by partial oxidation due to lower chemical robustness of $Nb@Si_{16}$ compared to $V@Si_{16}$ and $Ta@Si_{16}$, as discussed later on.

For the central metal atoms of V, Nb, and Ta, a couple of XPS peaks are distinctly observed due to the spin-orbit splittings of core levels (V: $2p_{1/2,3/2}$, Nb: $3d_{3/2,5/2}$, and Ta: $4f_{5/2,7/2}$). Similarly to
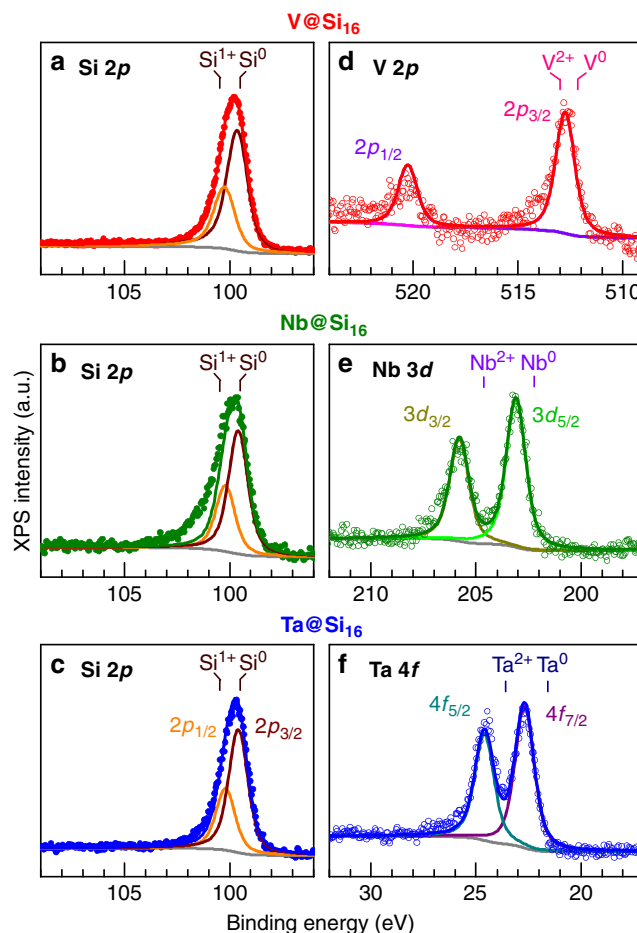
Si 2p, the peaks are reproduced by a single component using the spectroscopic parameters of energy separations and branching ratios of 2J+1; 7.5 eV, 2:1 for V $2p$[45], 2.8 eV, 3:2 for Nb 3d[46], and 1.915 eV, 4:3 for Ta $4f$[47]. Strictly speaking, both V 2p and Nb 3d peaks show a slight asymmetry with tailing components at a higher binding energy, whereas the Ta 4f peaks can be accurately fitted with a symmetric peak function. The tail structures in XPS spectra are seemingly caused not by a partial oxidation of the sample but by a photoelectron energy loss with a subsequent electron-hole excitation[48], which occurs more effectively at low photoelectron kinetic energy, E_k (higher binding energy). In fact, (1) an XPS spectrum for a standard sample of an Ag crystal, which has 3d derived core level at around 370 eV in binding energy ($E_k \approx 880$ eV), shows asymmetric features (Supplementary Figure 4), and (2) the XPS spectra taken with the Mg Kα line for the clean surfaces of V, Nb, and Ta have similar spectral widths for V 2p ($E_k \approx 740$ eV) and Nb 3d ($E_k \approx 1040$ eV) core levels but not for Ta 4f ($E_k \approx 1230$ eV)[46,49,50]. Therefore, the XPS spectra in Fig. 2 indicate that the chemical environments of both V and Nb in $M@Si_{16}$ are also uniform, similarly to $Ta@Si_{16}$, showing that all $M@Si_{16}$ superatoms deposited preserve the original metal encapsulating Si_{16} cage structures on a C_{60} substrate. From a theoretical perspective, Sen et al. recently calculated the structure of neutral $Ta@Si_{16}$ attaching to a graphite substrate, where all Ta

−Si distances are similar (2.85−2.97 Å), thereby resulting in a single and uniform chemical component of Si 2p and Ta 4f core levels[41]. The calculation reasonably supports the above conclusion in the present C_{60} substrate.

To compare the uniformity of chemical environments with a "nonencapsulating" metal-silicon nanocluster, we chose $TaSi_8^+$; eight Si atoms insufficient to encapsulate a Ta atom[51]. Accordingly, $TaSi_8^+$ cations were deposited onto a C_{60} substrate (Supplementary Figure 5), using MSP conditions that slightly enhance $TaSi_8^+$ cation formation (Supplementary Figure 6). For the $TaSi_8$ deposited film, indeed, the XPS peaks for Si 2p and Ta 4f are fitted by broader peak functions (1.66 eV for Si 2p and 1.36 eV for Ta 4f in FWHM, see Supplementary Figure 5), which is 1.52−1.25 times broader than those of $Ta@Si_{16}$. Together with the shift of the peak position towards a higher binding energy, the peak broadenings show inhomogeneous chemical environments of Si and Ta atoms due to the nonencapsulating structure of $TaSi_8$. In other words, the uniform chemical environment in $M@Si_{16}$ on a C_{60} substrate reveals the presence of the symmetric metal-encapsulating feature of the Si_{16} cage.

The charge state of the Si and central metal atoms are worth discussing to emphasize the characteristics of the alkali-like $M@Si_{16}$. As shown in the right hand of Fig. 2, since the peaks of metal core levels appear between metallic (M^0) and divalent (M^{2+}) charge states[45–47,52,53], the charge state of each central metal atom is assignable to monovalent (M^+), although such monovalent compounds of group-5 transition metals are rarely seen in the nature. Since the surrounding Si atoms are in a neutral charge state (Si^0) (Fig. 2a−c), the overall charge state of $M@Si_{16}$ is characterized to be +1 (namely $M@Si_{16}^+$), which favorably satisfies the 68 e^- shell closure for $M@Si_{16}$ with group 5 central metals. On the other hand, the C 1s peak shifts towards lower binding energy with depositing the $M@Si_{16}$ (Supplementary Figure 7). The results show that C_{60} is negatively charged due to a high electron affinity (2.68 eV) of C_{60} (n-type organic semiconductor)[54], forming a charge transfer (CT) complex of $M@Si_{16}+C_{60}^{-}$[37,38,40]. Furthermore, the stoichiometric ratio between $M@Si_{16}$ and C_{60} is 1:1 ($M@Si_{16}+C_{60}^-$) because the coverage dependence of the XPS/UPS spectra exhibits peak shift behaviors that saturated at 1 ML (Supplementary Figures 1, 2).

Oxidative reaction of $M@Si_{16}$. As shown in Fig. 2, the extra chemical component is observed in the Si 2p XPS signal for $Nb@Si_{16}$, implying that the chemical robustness of $M@Si_{16}$ is dependent on the central metal atom. Indeed, only for $Nb@Si_{16}$ is the Si 2p profile sensitive to change during the XPS measurements which irradiate trace amount of atomic oxygen from the X-ray source (Supplementary Figure 8). Chemical robustness is an important issue in the characterization of the alkali-like superatom family for Si-based nanomaterials. Here, we evaluate the chemical robustness of $M@Si_{16}$ as their oxidative reactivities towards a reactive gas of O_2, where both XPS profiles for Si 2p and the central metal core levels are obtained after step-by-step O_2 exposures at room temperature. The amount of oxygen is defined by Langmuir (1 L = an exposure of $1.33×10^{-4}$ Pa during 1 s). For every 1 L exposure, an O_2 molecule hits the $M@Si_{16}$ on the substrate approximately two times. As shown in Fig. 3, at $1×10^4$ L exposure, the original peak components for Si 2p and the central metal M are mostly retained, showing the enhanced chemical robustness of $M@Si_{16}$ on C_{60}. This compares with the behavior of clean crystalline Si surfaces as well as those of the central metal elements which are easily oxidized by less than 10 L oxygen exposure[55–61]. In particular, the enhanced chemical robustness of "*Si surface*" at $M@Si_{16}$ is worth comparing quantitatively with that at naked crystalline Si, whose oxidative reactivity towards oxygen has been extensively studied with many surface science techniques[55–58]. Through oxygen exposure, the multiple oxidation stages of Si atoms (e.g. Si^{1+}−Si^{4+}) are formed in both $M@Si_{16}$ (see next section) and bulk Si surfaces. Here the chemical robustness towards oxygen for $M@Si_{16}$ is considered as an XPS intensity ratio between unreacted Si (Si^0) and reacted Si (Si^{1+}−Si^{4+}, denoted $Si^{1~4+}$ in Fig. 4) after oxygen exposures.
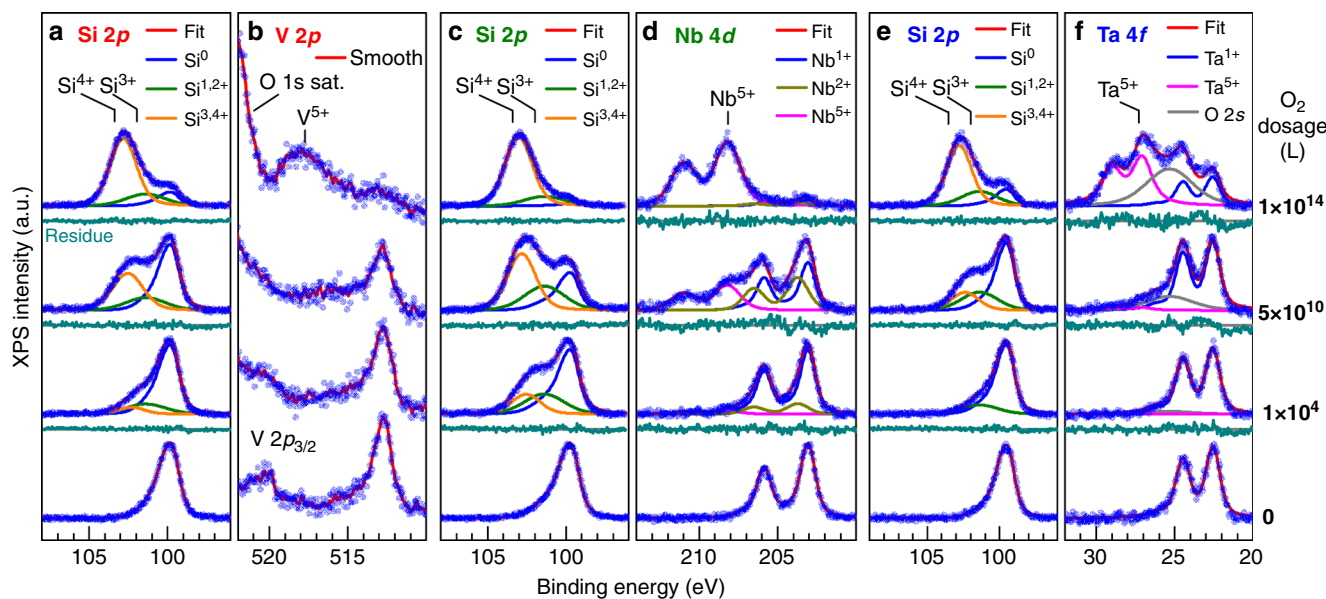

Fig. 3 XPS spectra for $M@Si_{16}$ deposited on a C_{60} substrate measured after different O_2 exposures. The XPS spectra obtained before and after O_2 exposures for $V@Si_{16}$ (**a** Si 2p and **b** V 2p), $Nb@Si_{16}$ (**c** Si 2p and **d** Nb 3d), and $Ta@Si_{16}$ (**e** Si 2p and **f** Ta 4f), where the amounts of O_2 exposures are defined as Langmuir (L). All spectra shift towards higher binding energy with oxygen exposures, indicating the $M@Si_{16}$ are oxidized and finally proceed to SiO_2 and M_2O_5 species. Reference binding energies of oxidized Si (Si^{3+} and Si^{4+}) and M (M^{5+}) are marked by vertical bars. The spectra of Si 2p are deconvoluted into three components of initial (Si^0), intermediate ($Si^{1,2+}$), and final ($Si^{3,4+}$) ones. For the metals, the spectra are dominated by M^+ and M^{5+} components, although for Nb 3d, the spectra are deconvoluted with Nb^{2+} as well as Nb^+ and Nb^{5+}. For Ta 4f, an O 2s contribution is also considered in the deconvolution. More details of the fitting procedures are seen in Supplementary Note 1

This simple assumption is considered valid because all Si atoms in M@Si$_{16}$ are equally exposed to oxygen in the present dispersive immobilization on the C$_{60}$ substrate. From an XPS study of the oxidation of Si single crystal surfaces, it has been reported that 80% of the surface Si atoms react with oxygen by 5 L O$_2$ exposure, thereby showing oxidized Si (Si^{1+}−Si^{4+})-derived peak components[55]. As analyzed in the next section, for M@Si$_{16}$, it shows only 20% (Ta@Si$_{16}$)−50% (Nb@Si$_{16}$) of the oxidized Si atoms after 1×10^4 L O$_2$ exposures (Si$^{1\sim4+}$ in Fig. 4). Compared to the case of a bulk Si surface, approximately one-fourth of the oxidative reaction occurs at the Si atoms of Ta@Si$_{16}$ despite 2×10^3 times higher oxygen dosages. By metal-encapsulation of Si$_{16}$ cage, therefore, the chemical robustness of the Si surface towards oxygen is enhanced by a factor of 10^4.

At 5×10^{10} L (=1 atm × 60 s), some changes in the Si 2p signal are evident. However, the spectra of central metal M mostly retain their original profiles, showing that the metal atom is still protected against oxidation by the partially oxidized Si$_{16}$ cage. The enhanced stability by the metal encapsulation suggests that air exposure within a few minutes lead to insignificant degradation of M@Si$_{16}$. In fact, a "nonencapsulating" TaSi$_8$ nanocluster obviously shows substantial reactivity towards the oxygen (Supplementary Figure 9); most of Si and Ta atoms react with oxygen at 5×10^{10} L.

By an extreme exposure of M@Si$_{16}$ to 1×10^{14} L (=1 atm × 40 h) oxygen, the main Si 2p and metal core peaks completely shift towards higher binding energies, whose charge states are Si^{3+} or Si^{4+}, and M^{5+}, respectively, as marked in Fig. 3[44,45,53,61]. The results indicate that the deposited M@Si$_{16}$ is finally oxidized into SiO$_2$ and M$_2$O$_5$ in the O$_2$-rich atmosphere, where the oxidation of the central metals is associated with the coreless structure as a final product. The detailed mechanism of the oxidative reaction, and the degree of reactivity of the central atoms are discussed as follows.

Mechanism of oxidative reaction on M@Si$_{16}$. As described previously, the O$_2$ exposure dependences are different between outer Si and inner central metal atoms. The surrounding 16 Si atoms exhibit initial oxidation showing an intermediate charge state of Si^{1+}−Si^{2+} (noted as Si$^{1,2+}$), and finally reach an oxidation state of Si^{3+}−Si^{4+} states (noted as Si$^{3,4+}$). On the other hand, the initial oxidation state of the metal atom (M^{1+}) is promptly changed into the final oxidation state of M^{5+}. In order to discuss the mechanism of oxidative reaction on M@Si$_{16}$, the XPS spectra of Fig. 3 are deconvoluted using three components of Si^0, Si$^{1,2+}$, and Si$^{3,4+}$ for Si 2p and two components of M^{1+} and M^{5+} for core levels of M. As shown in Fig. 3, the XPS spectra can be deconvoluted well, although for Nb@Si$_{16}$, the minor intermediate component of Nb^{2+} has to be included (see Supplementary Note 1 for details).

Figure 4 shows the ratios of the Si^0, Si$^{1,2+}$, and Si$^{3,4+}$ states, and that of the M^{1+} and M^{5+} states against oxygen dosages. For Si 2p of all M@Si$_{16}$, it is clear that the oxidation proceeds as a sequential two-step reaction via the intermediate oxidation states of Si$^{1,2+}$, and then the Si$^{3,4+}$ component appears at higher oxygen exposures. For the oxidation of the metal atom, the XPS peaks exhibit a behavior indicating a primary reaction where the rise of M^{5+} is followed by the decay of M^{1+}. Since the intensity evolutions of M^{5+} closely correspond to those for the Si$^{3,4+}$ component, the intermediate states of Si$^{1,2+}$ are ascribed to Si$_{16}$ cage oxidation, keeping the metal atom protected, such as with 2O adducts via dissociative O$_2$ adsorption products (Supplementary Figure 10), and those of Si$^{3,4+}$ are resulted from the Si$_{16}$ cage collapse along with metal oxidation. Note that, for the Nb@Si$_{16}$, the minor intermediate oxidized component of Nb 4$d_{5/2}$ at 203.7
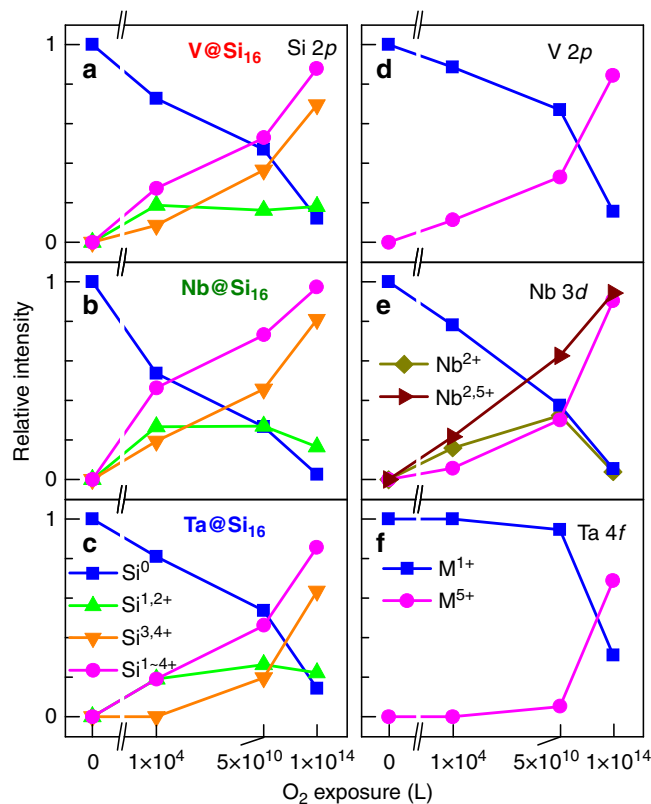

Fig. 4 Area ratio of spectral components of Si 2p and core levels of M. The initial (Si^0), intermediate (Si$^{1,2+}$), and final (Si$^{3,4+}$) charge states for Si 2p for **a** V@Si$_{16}$, **b** Nb@Si$_{16}$, and **c** Ta@Si$_{16}$, and initial (M^{1+}) and final (M^{5+}) charge states for core levels of **d** V@Si$_{16}$ (V 2p), **e** Nb@Si$_{16}$ (Nb 3d), and **f** Ta@Si$_{16}$ (Ta 4f) are obtained from the analysis of XPS spectra in Fig. 3. The summation of Si$^{1,2+}$ and Si$^{3,4+}$ (solid pink circles) is also shown. With increasing oxygen exposure, for Si 2p, the intermediate states of Si$^{1,2+}$ (solid green triangles) increase at first, and then Si$^{3,4+}$ (solid orange triangles) dominates at higher O$_2$ exposures. The intensity evolutions of M^{5+} (including M^{2+} for Nb 4d) are similar to ones for Si$^{3,4+}$, corresponding to Si cage collapse

eV, corresponding to the binding energy of NbO (Nb^{2+})[60], is extracted in the fitting procedure owing to the higher reactivity of Nb@Si$_{16}$, where Nb oxidation seemingly progresses as the Si cage collapses.

From the above intensity analysis, it is fair to conclude that the surrounding Si atoms are oxidized initially preserving the caged structure, and then the caged structure collapses, resulting in the highest oxidation states like SiO$_2$ and M$_2$O$_5$. The maximum intensity ratio of the Si$^{1,2+}$ component is about 30%, implying that the number of oxygen atoms attached is 4−5 per M@Si$_{16}$ before the collapse of the Si$_{16}$ cage. The experimental observation is in fair agreement with the theoretical work by Sen et al., who suggest from their calculation that: (1) in the oxidation reaction of Ta@Si$_{16}$ cage, the central Ta atom is protected by the surrounding 16 Si atoms from the oxygen, and (2) six Si atoms (38% of 16 Si atoms) in Ta@Si$_{16}$ are affected by four oxygen molecules in a possible final structure after exposure[41].

In the oxidation of crystalline Si surfaces it is well-known that O$_2$ molecules dissociatively chemisorb on the top Si atoms at room temperature as atomic O, which forms the oxidized surface in a "Si-O-Si" bridging configuration[44,56−58,62−64]. Further oxidation (formation of a SiO$_2$ film) is followed by the oxygen penetrating deep into the Si surface, accompanying the thermal evaporation of molecular SiO to relax lattice mismatches[65,66]. The

M@Si$_{16}$ superatoms are similarly oxidized by atomic oxygen dissociatively adsorbed on the Si$_{16}$ cage, because during initial oxidation (1×10^4 L) the XPS peak of the O 1s core level shows almost the same binding energy (532.3 eV for Ta@Si$_{16}$ on C$_{60}$) with that observed in the first oxidative product of SiO at crystalline Si surfaces with O$_2$ exposure (see Supplementary Figure 11)[62]. On the crystalline Si surface, further oxidation followed by oxygen penetration deeper into the surface results in a slight energy shift of the O 1s core level towards a higher binding energy by 0.55 eV (in pure SiO$_2$)[62]. In fact, the O 1s core level for Ta@Si$_{16}$ on C$_{60}$ (Supplementary Figure 11) consistently shifts by 0.35 eV towards a higher binding energy at an O$_2$ exposure of 1×10^{14} L compared with that at 1×10^4 L. The results show that the final product of the oxidized Si$_{16}$ cage is mainly SiO$_2$ compounds without any bonding to the central metal atom.

The structural dynamics in the M@Si$_{16}$ oxidation are discussed from the total XPS intensity analysis of Si 2p with O$_2$ exposure. Figure 5 displays the integrated intensities of core levels at each O$_2$ exposure, in which the XPS signal intensity is carefully normalized (Supplementary Figure 12). The Si 2p intensities (Fig. 5a) for all M@Si$_{16}$ increase with O$_2$ exposure, and the Si 2p signals are enhanced to 125−135%. At a coverage of M@Si$_{16}$ of 0.6 ML, the enhancement is ascribed to a cage collapse of M@Si$_{16}$ via an oxidative reaction, which is caused by the extension of the mean Si surface area with relief of the attenuation of photoemission from the back half of the Si$_{16}$ cage. In fact, as mentioned above, the dosage dependences of Si$^{3,4+}$ and M^{5+} in Fig. 4 are similar to each other, and moreover their behaviors are similar also to the dosage dependence of the total Si 2p intensities in Fig. 5b. The results consistently show Si cage collapse at the higher O$_2$ dosages. Concurrently, the intensity enhancement of Si 2p indicates that the oxidation of M@Si$_{16}$ occurs without SiO desorption, although the oxidation of bulk Si surface is accompanied by desorption of SiO[65,66].

Although the XPS analyses of the central metals contain some uncertainties due to satellites (in V 2p and Nb 4d) and O 2s contributions (in Ta 4f) (see Supplementary Figure 12), the XPS intensities of the metals increase slightly against the O$_2$ dosage by 120% at most (Fig. 5b). The result suggests that the metal atoms are unsealed from the Si cage, as described in detailed discussion in Supplementary Note 2.

Periodicity of chemical stability for M@Si$_{16}$.

Although the oxidation robustness of M@Si$_{16}$ compounds are distinct compared to naked Si surfaces, the degree of robustness depends on the central metal atom; Ta@Si$_{16}$ > V@Si$_{16}$ > Nb@Si$_{16}$, as seen in Figs. 3, 4. Here we evaluate the rate constant of M@Si$_{16}$ oxidation, k_M (M = V, Nb, and Ta), assuming that (1) the oxidation proceeds with step-by-step attachment of oxygen molecules, and (2) the $k_{M@Si16}$ of each oxidation step is identical at an early stage of oxygen exposure (1×10^4 L). These assumptions are known as the Eley-Rideal mechanism[67], where gas phase molecules directly react with adsorbed species. Importantly, the kinetic analyses are valid when the M@Si$_{16}$ superatoms are immobilized monodispersively on a surface. In fact, the C$_{60}$ decoration makes the M@Si$_{16}$ superatoms individually immobilized due to local chemical interactions of a CT nature between M@Si$_{16}$ and C$_{60}$, which has been examined by STM[37,38].

By exposing oxygen molecules to deposited M@Si$_{16}$, the Si$_{16}$ cage is oxidized sequentially to M@Si$_{16}$O$_{2n}$, where dissociative O$_2$ adsorption plausibly produces 2O adducts as shown in Supplementary Figure 10, similarly to bulk Si surface oxidation[63,64]. Along the stepwise oxidation of M@Si$_{16}$ → M@Si$_{16}$O$_2$ → M@Si$_{16}$O$_4$ → …, some of the Si 2p XPS signal shifts from Si^0 to Si$^{1,2+}$, and the drop of the Si^0 component in Fig. 4 indicates the

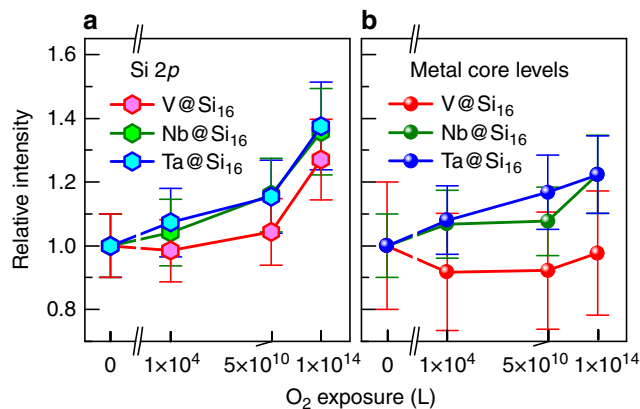**Fig. 5** Total XPS intensities at each oxygen dosage. The XPS intensities of **a** Si 2p and **b** metals core levels for V@Si$_{16}$, Nb@Si$_{16}$, and Ta@Si$_{16}$. The intensity fluctuations of the X-ray source are normalized by the XPS signal at a binding energy of 110 eV, where background signals are obtained that only vary with the light intensity. The detailed procedures and the XPS data are shown in Supplementary Figure 12. Error bars: the uncertainty in the intensity analysis is estimated to be ±10%, except for V 2p (±20%). The Si 2p signals for all M@Si$_{16}$ increase with oxygen exposures, and are 1.25−1.35 times stronger at >1×10^{14} L than that of as-deposited ones, implying Si cage collapse of M@Si$_{16}$. The changes of the core levels of the central metals are less significant compared to the Si 2p because M atoms are located beneath a layer of Si

progress of oxidation reaction in units of L. Since the exposure amount can be converted to the corresponding reaction time under elementary reactions, the reaction rates, $k_{M@Si16}$, are qualitatively evaluated by the conversion of 1 L → 1 s. At 1×10^4 L, the ratio of nonoxidized Si atoms (Si^0), $R_{M@Si16}$, are $R_{V@Si16}$ = 0.73, $R_{Nb@Si16}$ = 0.54, and $R_{Ta@Si16}$ = 0.81 (Fig. 4a−c), and thus these ratios provide $k_{V@Si16} = 1.4\times10^{-4}$/s, $k_{Nb@Si16} = 2.5\times10^{-4}$/s, and $k_{Ta@Si16} = 1.0\times10^{-4}$/s (see Supplementary Note 3 and Supplementary Figure 13 for details).

The difference in chemical reactivities, depending on the central metal atoms, can be discussed in terms of electronic properties of free M@Si$_{16}$ superatoms obtained from DFT calculations, in which an electron transfer from M@Si$_{16}$ superatom to O$_2$ molecules is described as a key process in the dissociative O$_2$ adsorption[58,63,64]. When the second ionization energies are calculated for M@Si$_{16}$ corresponding to the ionization energy (E_i) of cationic M@Si$_{16}^+$, they are calculated as: E_i(V@Si$_{16}^+$); 10.93 > E_i(Nb@Si$_{16}^+$); 10.90 > E_i(Ta@Si$_{16}^+$); 10.87 in eV. This energetic parameter is important for reaction of O$_2$ as postulated for metal nanoclusters[35]. Although the delicate difference in the second E_is implies that Ta@Si$_{16}$ is most reactive for Ta@Si$_{16}^{2+}$O$_2^-$ formation, the second ionization energy appears to be an implausible argument to explain the reactivity difference. In terms of reaction energetics, the binding energies for the molecular adduct of ^{3}[M@S$_{16}$ − (O$_2$)] and the dissociated adduct of ^{1}[M@S$_{16}$(O)$_2$] gradually decrease with decreasing period number of the central metal (Supplementary Figure 10), by which the nonperiodic trend for Nb@Si$_{16}^+$ could not be explained. Since the oxidation reaction proceeds through spin-flip from the initially formed ^{3}[M@Si$_{16}$(O$_2$)]$^+$ to the dissociated product of ^{1}[M@Si$_{16}$(O$_{dis}$)$_2$]$^+$ (Supplementary Figure 10), the HOMO-LUMO gaps of the nanoclusters correspond well with spin excitation energy from the initial state is also important[35]. However, the calculated HOMO-LUMO gaps for M@Si$_{16}^+$ (3.99 eV for M = Ta, 3.99 eV for M = Nb, and 3.88 eV for M = V) never correlate with the observed reactivity trend. Since the initial step of the molecular O$_2$ adsorption on M@Si$_{16}^+$
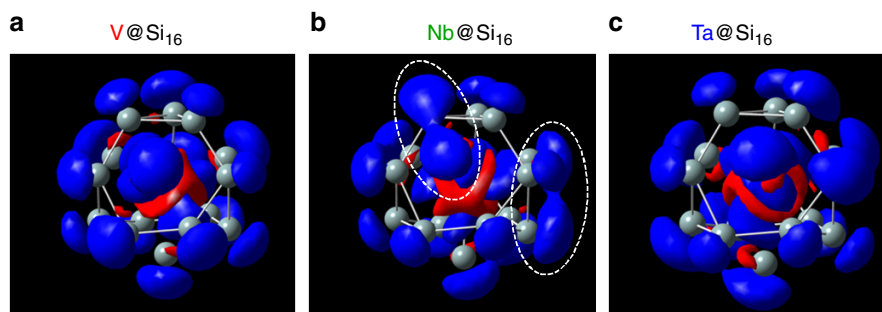
Fig. 6 Isosurfaces for the difference electron density between $M@Si_{16}^+$ and $M@Si_{16}^{2+}$. Those for **a** M = V, **b** Nb, and **c** Ta are calculated with the def-TZVP basis set, where the blue (red) region corresponds to the decrease (increase) of electron density difference ($\Delta\rho$) at $\Delta\rho < -0.0008$ e$^-$/a.u.^{3} ($\Delta\rho > +0.0008$ e$^-$/a.u.^{3}). In the calculations, the geometric structure is fixed to that optimized one for $M@Si_{16}^+$. The decrease of $\Delta\rho$ outside the Si cage is significant in $Nb@Si_{16}$, as shown by circles with dotted lines

seems sensitive to the degree of electron density spreading to the outside of the Si_{16} cage, the electron density was also calculated. For alkali metal atoms of K, Rb, and Cs, indeed, the ns electrons spread more in higher quantum number orbitals (K ($4s$) < Rb ($5s$) < Cs ($6s$)) with a lowering of E_is, and their oxidation reactivity becomes greater with heavier alkali atoms.

Figure 6 shows the calculated difference of total electron density ($\Delta\rho$) between monocationic $M@Si_{16}^{1+}$ and dicationic $M@Si_{16}^{2+}$ for M= (a) V, (b) Nb, and (c) Ta. The blue and red regions show the increase ($\Delta\rho > +0.0008$ e$^-$/a.u.^{3}) and decrease ($\Delta\rho < -0.0008$ e$^-$/a.u.^{3}) of electron density, respectively, by changing the charge state from $M@Si_{16}^{1+}$ to $M@Si_{16}^{2+}$, where the geometric frameworks are fixed to the optimized monocationic species. Since the charge distributions approximately correspond to an electron transfer channel to form an O_2^- adduct, the distribution seems relevant to the oxidation reactivity. Although the spatial shapes of $\Delta\rho$ distribution are similar to each other, it is clear that the electrons in $Nb@Si_{16}$ spread further outside the Si frame (marked by a dotted line) compared to $V@Si_{16}$ and $Ta@Si_{16}$. This is presumably because the central metal's d-orbitals contributing to the superatomic molecular orbitals of $M@Si_{16}$ are distinctly delocalized over the Si_{16} cage, seemingly resulting in the higher chemical reactivity. The results show that the chemical properties of $M@Si_{16}$ superatoms are governed not only by the electron counting rule (68 e$^-$) but also by the species of the central metal hybridized with the Si_{16} cage.

Discussion

Our results demonstrate that the oxidation reactivities of alkali-like $M@Si_{16}$ nanocluster superatoms deposited on a C_{60} surface are characterized for M = V, Nb, and Ta using XPS spectra. The nanostructured metal–atom encapsulation makes Si atoms in a gas or a surface compound much less reactive with oxygen molecules by a factor of 10^4, particularly when $M@Si_{16}$ forms a charge transfer complex with a C_{60} molecule as $M@Si_{16}^+C_{60}^-$, where $M@Si_{16}^+$ satisfies an electronically closed superatom of 68 e$^-$. The oxidation proceeds stepwise via the oxidation of the Si_{16} cage and finally results in fully oxidized SiO_2 and M_2O_5 with the collapse of the cage. The chemical reactivities of $M@Si_{16}$ depends on the central metal atom; $Nb@Si_{16} > V@Si_{16} > Ta@Si_{16}$, which is explained by the degree of electron density spreading outside the $M@Si_{16}$ obtained by the DFT calculation. Since the nature revealed as a periodic dependence in a superatom periodic table is closely related to a transfer integral in their aggregates, this periodic variation in chemical and physical properties may inspire

scientists to design assembled functional nanomaterials consisting of naked $M@Si_{16}$ superatoms.

Methods

Nanocluster generation and deposition. $M@Si_{16}$ nanoclusters were generated by an MSP technique, whose detailed experimental configuration has been described elsewhere[37–40]. Briefly, M−Si alloy targets were sputtered and clusterized in an aggregation cell with a cooled He flow. The cationic nanocluster beam involving $M@Si_{16}^+$ was introduced to a quadrupole mass filter through ion optics. The $M@Si_{16}$ superatoms were deposited on to the substrate of 2 ML C_{60} film formed on highly oriented pyrolytic graphite. The collision energy of $M@Si_{16}^+$ to the substrate was set to as low as possible by applying the voltages to the substrate (soft landing condition), which was typically less than 2 eV per cluster. The amount of deposition was monitored with a pico-ammeter and was controlled to be 2.9×10^{13} nanoclusters except for the coverage dependence experiment, which is equal to 0.6 ML coverage, assuming a deposition area of 6 mm in diameter and the size of $M@Si_{16}$ (0.8–0.9 nm diameter)[37]. The deposited samples were transferred to the photoelectron spectroscopy system connecting with the MSP nanocluster deposition system while keeping ultrahigh vacuum conditions. The morphology of the $M@Si_{16}^+$ deposited surface was confirmed by STM, where the $Ta@Si_{16}^+$ nanoclusters are independently immobilized on the C_{60} surface[37,38].

Photoelectron spectroscopy. XPS measurements were performed using an Mg Kα ($h\nu = 1253.6$ eV) X-ray source. Photoelectrons emitted from the sample were collected with a commercial hemispherical electron analyzer (VG SCIENTA, R-3000), where the detection angle was 45° from the surface normal. In the XPS analysis, the peak fittings were performed using an instrumental broadening as a Voigt function (FWHMs amounted to 1.09 eV, for which Gaussian and Lorentzian components equaled 0.75 and 0.56 eV, respectively), after a subtraction of the Shirley background. The sample temperature during all XPS measurements was kept to room temperatures.

Calculations. All geometries of $M@Si_{16}^+$ (M = V, Nb, and Ta) nanocluster cations and their oxygen adducts of $[M@Si_{16}O]^+$ and $[M@Si_{16}O_2]^+$ were optimized by the density functional incorporated in the Gaussian09 program[68] until no imaginary frequency was found. The hybrid exchange-correlation functional of PBE0[69] and triple-zeta valence basis function of def-TZVP[70] were utilized in the calculations. Difference electron density isosurfaces were visualized with GaussView5 based on the difference between the total electron density for $M@Si_{16}^+$ (optimized structure) and $M@Si_{16}^{2+}$ (same structure with monovalent cation).

References

1. Peercy, P. S. The drive to miniaturization. *Nature* **406**, 1023–1026 (2000).
2. Flood, A. H., Stoddart, J. F., Steuerman, D. W. & Heath, J. R. Whence molecular electronics? *Science* **306**, 2055–2056 (2004).

3. Ito, T. & Okazaki, S. Pushing the limit of lithography. *Nature* **406**, 1027–1031 (2000).

4. Schmidt, V., Wittemann, J. V., Gösele, U., Bley, R. A. & Kauzlarich., S. M. A low-temperature solution phase route for the synthesis of silicon nanoclusters. *J. Am. Chem. Soc.* **118**, 12461–12462 (1996).

5. Morales, A. M. & Lieber, C. M. A laser ablation method for the synthesis of crystalline semiconductor nanowires. *Science* **279**, 208–211 (1998).

6. De Padova, P. et al. Burning match oxidation process of silicon nanowires screened at the atomic scale. *Nano Lett.* **8**, 2299–2304 (2008).

7. Sugiyama, Y. et al. Synthesis and optical properties of monolayer organosilicon nanosheets. *J. Am. Chem. Soc.* **132**, 5946–5947 (2010).

8. Okamoto, H., Sugiyama, Y. & Nakano, H. Synthesis and modification of silicon nanosheets and other silicon nanomaterials. *Chem. Eur. J* **17**, 9864–9887 (2011).

9. Yaokawa, R. et al. Monolayer-to-bilayer transformation of silicenes and their structural analysis. *Nat. Commun.* **7**, 10657 (2016).

10. Kara, A. et al. A review on silicene-new candidate for electronics. *Surf. Sci. Rep.* **67**, 1–18 (2012).

11. De Padova, P., Quaresima, C., Olivieri, B., Perfetti, P. & Le Lay, G. Strong resistance of silicene nanoribbons towards oxidation. *J. Phys. D. Appl. Phys.* **44**, 312001 (2011).

12. Molle, A. et al. Hindering the oxidation of silicene with non-reactive encapsulation. *Adv. Funct. Mater.* **23**, 4340–4344 (2013).

13. Cerdá, J. I. et al. Unveiling the pentagonal nature of perfectly aligned single- and double-strand Si nano-ribbons on Ag(110). *Nat. Commun.* **7**, 13076 (2016).

14. Zybill, C. Si₆₀, an analogue of C₆₀? *Angew. Chem. Int. Ed.* **31**, 173–175 (1992).

15. Bower, J. E. & Jarrold, M. F. Properties of deposited size-selected clusters: reactivity of deposited silicon clusters. *J. Chem. Phys.* **97**, 8312–8321 (1993).

16. Li, B.-X. & Cao, P. L. Distorted cage structures of Sin (n=20, 24, 26, 28, 30, 32) clusters. *J. Phys. Condens. Matter* **13**, 10865–10872 (2001).

17. Yoo, S., Zhao, J., Wang, J. & Zeng, X. C. Endohedral silicon fullerenes Si$_N$ (27 ≤ N ≤ 39). *J. Am. Chem. Soc.* **126**, 13845–13849 (2004).

18. Kumar, V. & Kawazoe, Y. Metal-encapsulated fullerenelike and cubic caged clusters of silicon. *Phys. Rev. Lett.* **87**, 045503 (2001).

19. Khanna, S. N., Rao, B. K. & Jena, P. Magic numbers in metallo-inorganic clusters: chromium encapsulated in silicon cages. *Phys. Rev. Lett.* **89**, 016803 (2002).

20. Kawamura, H., Kumar, V. & Kawazoe, Y. Growth behavior of metal-doped silicon clusters Si$_n$M (M=Ti, Zr, Hf; n=8–16). *Phys. Rev. B* **71**, 075423 (2005).

21. Reveles, J. U. & Khanna, S. N. Nearly-free-electron gas in a silicon cage. *Phys. Rev. B* **72**, 165413 (2005).

22. Zheng, W., Nilles, J. M., Radisic, D. & Bowen, K. H. Jr. Photoelectron spectroscopy of chromium-doped silicon cluster anions. *J. Chem. Phys.* **122**, 071101 (2005).

23. Koyasu, K., Akutsu, M., Mitsui, M., & Nakajima, A. Selective formation of MSi₁₆ (M=Sc, Ti, and V). *J. Am. Chem. Soc.* **127**, 4998–4999 (2005).

24. Jaeger, J. B., Jaeger, T. D. & Duncan, M. A. Photodissociation of metal-silicon clusters: encapsulated versus surface-bound metal. *J. Phys. Chem. A* **110**, 9310–9314 (2006).

25. Reveles, J. U. & Khanna, S. N. Electronic counting rules for the stability of metal-silicon clusters. *Phys. Rev. B* **74**, 035435 (2006).

26. Torres, M. B., Fernández, E. M. & Balbás, L. C. Theoretical study of isoelectronic Si$_n$M clusters (M=Sc, Ti, V⁺, n=14-18). *Phys. Rev. B* **75**, 205425 (2007).

27. Koyasu, K., Atobe, J., Akutsu, M., Mitsui, M. & Nakajima, A. Electronic and geometric stabilities of clusters with transition metal encapsulated by silicon. *J. Phys. Chem. A* **111**, 42–49 (2007).

28. Lau, J. T. et al. X-ray spectroscopy reveals high symmetry and electronic shell structure of transition-metal-doped silicon clusters. *Phys. Rev. A* **79**, 054301 (2009).

29. Cantera-López, H., Balbás, L. C. & Borstel, G. First-principles calculations of structural and electronic properties of Ta-doped Si clusters, wires, and bulk systems. *Phys. Rev. B* **83**, 075434 (2011).

30. Jena, P. Beyond the periodic table of elements: the role of superatoms. *J. Phys. Chem. Lett.* **4**, 1432–1442 (2013).

31. Abreu, M. B., Reber, A. C. & Khanna, S. N. Does the 18-electron rule apply to CrSi₁₂? *J. Phys. Chem. Lett.* **5**, 3492–3496 (2014).

32. Chauhan, V., Abreu, M. B., Reber, A. C. & Khanna, S. N. Geometry controls the stability of FeSi₁₄. *Phys. Chem. Chem. Phys.* **17**, 15718–15724 (2015).

33. Tomalia, D. A. & Khanna, S. N. A systematic framework and nanoperiodic concept for unifying nanoscience: hard/soft nanoelements, superatoms, meta-atoms, new emerging properties, periodic property patterns, and predictive Mendeleev-like nanoperiodic tables. *Chem. Rev.* **116**, 2705–2774 (2016).

34. Tsunoyama, H. et al. Development of integrated dry–wet synthesis method for metal encapsulating silicon cage superatoms of M@Si₁₆ (M=Ti and Ta). *J. Phys. Chem. C* **121**, 20507–20516 (2017).

35. Reber, A. C. & Khanna, S. N. Superatoms: electronic and geometric effects on reactivity. *Acc. Chem. Res.* **50**, 255–263 (2017).

36. Tsunoyama, H., Shibuta, M., Nakaya, M., Eguchi, T. & Nakajima, A. Synthesis and characterization of metal-encapsulating Si₁₆ cage superatoms. *Acc. Chem. Res.* https://doi.org/10.1021/acs.accounts.8b00085 (2018).

37. Nakaya, M., Iwasa, T., Tsunoyama, H., Eguchi, T. & Nakajima, A. Formation of a superatom monolayer using gas-phase-synthesized Ta@Si₁₆ nanocluster ions. *Nanoscale* **6**, 14702–14707 (2014).

38. Nakaya, M., Iwasa, T., Tsunoyama, H., Eguchi, T. & Nakajima, A. Heterodimerization via the covalent bonding of Ta@Si₁₆ nanoclusters and C₆₀ molecules. *J. Phys. Chem. C* **119**, 10962–10968 (2015).

39. Shibuta, M. et al. Chemical characterization of an alkali-like superatom consisting of a Ta-encapsulating Si₁₆ cage. *J. Am. Chem. Soc.* **137**, 14015–14018 (2015).

40. Ohta, T., Shibuta, M., Tsunoyama, H., Eguchi, T. & Nakajima, A. Charge transfer complexation of Ta-encapsulating Ta@Si₁₆ superatom with C₆₀. *J. Phys. Chem. C* **120**, 15265–15271 (2016).

41. Sen, A. & Sen, P. Properties of highly oriented pyrolytic graphite supported TaSi₁₆ clusters: a density functional investigation. *J. Phys. Chem. C* **121**, 28490–28497 (2017).

42. Zhang, C. et al. Advanced nanocluster ion source based on high-power impulse magnetron sputtering and time-resolved measurements of nanocluster formation. *J. Phys. Chem. A* **117**, 10211–10217 (2013).

43. Rangelov, G. & Fauster, Th Thermally-induced evolution of codeposited Co-Si layers on Si(100)surfaces. *Surf. Sci.* **365**, 403–410 (1996).

44. Himpsel, F. J., McFeely, F. R., Taleb-Ibrahimi, A., Yarmoff, J. A. & Hollinger, G. Microscopic structure of the SiO₂/Si interface. *Phys. Rev. B* **38**, 6084–6096 (1988).

45. Silversmit, G., Depla, D., Poelman, H., Marin, G. B. & Gryse, R. D. Determination of the V2p XPS binding energies for different vanadium oxidation states (V⁵⁺ to V⁰⁺). *J. Electron Spectrosc. Relat. Phenom.* **135**, 167–175 (2004).

46. Latta, E.-E. & Ronay, M. Catalytic oxidation of niobium by rare earths. *J. Vac. Sci. Technol. A* **4**, 1626–1630 (1986).

47. Riffe, D. M. & Wertheim, G. K. Ta(110) surface and subsurface core-level shifts and 4f₇/₂ line shapes. *Phys. Rev. B* **47**, 6672–6679 (1993).

48. Doniach, S. & Šunjić, M. Many-electron singularity in x-ray photoemission and x-ray line spectra from metals. *J. Phys. C: Solid St. Phys.* **3**, 285–291 (1970).

49. Kasperkiewicz, J., Kovacich, J. A. & Lichtman, D. XPS studies of vanadium and vanadium oxides. *J. Electron Spcectrosc. Relat. Phenom.* **32**, 123–132 (1983).

50. Atanassova, E. & Spassov, D. X-ray photoelectron spectroscopy of thermal thin Ta₂O₅ films on Si. *Appl. Surf. Sci.* **135**, 71–82 (1998).

51. Guo, P. et al. Relativistic computational investigation: the geometries and electronic properties of TaSi$_n$⁺ (n=1−13, 16) clusters. *J. Phys. Chem. A* **110**, 7453–7460 (2006).

52. Horvathj, B., Strutzj, J., Geyer-Lippman, J. & Horva, E. G. Preparation, properties, and ESCA characterization of vanadium surface compounds on silicagel. I. *Z. Anorg. Allg. Chem.* **483**, 181–192 (1981).

53. Ho, S. F., Contarini, S. & Rabalais, J. W. Ion-beam-induced chemical changes in the oxyanions (MO$_y$$^{n-}$) and oxides (MO$_x$) where M=Cr, Mo, W, V, Nb, and Ta. *J. Phys. Chem.* **91**, 4779–4788 (1987).

54. Huang, D. L., Dau, P. D., Liu, H. T. & Wang, L. S. High-resolution photoelectron imaging of cold C₆₀⁻ anions and accurate determination of the electron affinity of C₆₀. *J. Chem. Phys.* **140**, 224315 (2014).

55. Hollinger, G. & Himpsel, F. J. Multiple-bonding configurations for oxygen on silicon surfaces. *Phys. Rev. B* **28**, 3651–3653 (1983).

56. Höfer, U., Morgen, P., Wurth, W. & Unbach, E. Metastable molecular precursor for the dissociative adsorption of oxygen on Si(111). *Phys. Rev. Lett.* **55**, 2979–2982 (1985).

57. Morgen, P., Höfer, U., Wurth, W. & Unbach, E. Initial stages of oxygen adsorption on Si(111):the stable state. *Phys. Rev. B* **39**, 3720–3734 (1989).

58. Höfer, U., Morgen, P., Wurth, W. & Unbach, E. Initial stages of oxygen adsorption on Si(111). II. the molecular precursor. *Phys. Rev. B* **40**, 1130–1145 (1989).

59. Shen, M., Ma, Q., Lee, I. & Zaera, F. Oxygen adsorption and oxide formation on V(100) surfaces. *J. Phys. Chem. C* **111**, 6033–6040 (2007).

60. Hu, Z. P., Li, Y. P., Ji, M. R. & Wu, J. X. The interaction of oxygen with niobium studied by XPS and UPS. *Solid State Commun.* **71**, 849–852 (1989).

61. van der Veen, J. F., Himpsel, F. J. & Eastman, D. E. Chemisorption-induced 4f-core-electron binding-energy shifts for surface atoms of W(111), W(100), and Ta(111). *Phys. Rev. B* **25**, 7388–7397 (1982).

62. Hollinger, G., Jugnet, Y., Pertosa, P. & Duc., T. M. X-ray photoelectron spectroscopy of thermally grown silicon dioxide film on silicon. *Chem. Phys. Lett.* **36**, 441–445 (1975).

63. Lee, S.-H. & Kang, M.-H. Identification of the initial-stage oxidation products on Si(111)-(7 × 7). *Phys. Rev. Lett.* **82**, 968–971 (1999).

64. Lee, S.-H. & Kang, M.-H. Origin of O 1s core-level shifts on oxygen adsorbed Si(111)-(7 × 7). *Phys. Rev. Lett.* **84**, 1724–1727 (2000).

65. Engel, Th The interaction of molecular and atomic oxygen with Si(100) and Si (111). *Surf. Sci. Rep.* **18**, 93–144 (1993).

66. Raschke, M. B., Bratu, P. & Höfer, U. Optical second-harmonic investigations of the isothermal desorption of SiO from the Si(100) and Si(111)surfaces. *Surf. Sci.* **410**, 351–361 (1998).

67. Weinberg, W. H. Eley-Rideal surface chemistry: direct reactivity of gas phase atomic hydrogen with adsorbed species. *Acc. Chem. Res.* **29**, 479–487 (1996).

68. Frisch, M. J. et al. Gaussian 09, Revision E.01 (Gaussian, Inc., Wallingford CT, 2013).

69. Adamo, C. & Barone, V. Toward reliable density functional methods without adjustable parameters: The PBE0 Model. *J. Chem. Phys.* **110**, 6158–6170 (1999).

70. Schäfer, A., Horn, H. & Ahlrichs, R. Fully optimized contracted Gaussian basis sets of triple zeta valence quality for atoms Li to Kr. *J. Chem. Phys.* **100**, 5829–5835 (1994).

Acknowledgements

Author contributions

M.S., T.K., T.O., H. T., and A.N. contributed to the experimental process. M.S., H.T., and A.N. carried out the simulations and theoretical interpretations. All authors have given approval to the final version of the manuscript.

Additional information

Competing interests: The authors declare no competing interests.

Reprints and permission information is available online at http://npg.nature.com/reprintsandpermissions/

Publisher's note: Springer Nature remains neutral with regard to jurisdictional claims in published maps and institutional affiliations.